

Article

Development of Fluorescent Carbon Nanoparticle-Based Probes for Intracellular pH and Hypochlorite Sensing

Yu-Syuan Lin¹, Li-Wei Chuang¹ , Yu-Feng Lin¹, Shun-Ruei Hu¹, Chih-Ching Huang^{2,3,4} , Yu-Fen Huang^{4,5,6,*} and Huan-Tsung Chang^{1,*}

¹ Department of Chemistry, National Taiwan University, Taipei 10617, Taiwan; hero1245337@gmail.com (Y.-S.L.); abcdboony@gmail.com (L.-W.C.); assassin52852@gmail.com (Y.-F.L.); ick20140216@gmail.com (S.-R.H.)

² Department of Bioscience and Biotechnology, National Taiwan Ocean University, Keelung 20224, Taiwan; huanging@mail.ntou.edu.tw

³ Center of Excellence for the Oceans, National Taiwan Ocean University, Keelung 20224, Taiwan

⁴ School of Pharmacy, College of Pharmacy, Kaohsiung Medical University, Kaohsiung 80708, Taiwan

⁵ Institute of Analytical and Environmental Sciences, National Tsing Hua University, Hsinchu 30013, Taiwan

⁶ Department of Biomedical Engineering and Environmental Sciences, National Tsing Hua University, Hsinchu 30013, Taiwan

* Correspondence: yufen@mx.nthu.edu.tw (Y.-F.H.); changht@ntu.edu.tw (H.-T.C.)

Abstract: Acid-base and redox reactions are important mechanisms that affect the optical properties of fluorescent probes. Fluorescent carbon nanoparticles (CNPs) that possess tailored surface functionality enable a prompt response to regional stimuli, offering a useful platform for detection, sensing, and imaging. In this study, mPA CNPs were developed through one-pot hydrothermal reaction as a novel fluorescent probe (quantum yield = 10%) for pH and hypochlorite sensing. *m*-Phenylenediamine was chosen as the major component of CNPs for pH and hypochlorite responsiveness. Meanwhile, ascorbic acid with many oxygen-containing groups was introduced to generate favorable functionalities for improved water solubility and enhanced sensing response. Thus, the mPA CNPs could serve as a pH probe and a turn-off sensor toward hypochlorite at neutral pH through fluorescence change. The as-prepared mPA CNPs exhibited a linear fluorescence response over the pH ranges from pH 5.5 to 8.5 ($R^2 = 0.989$), and over the concentration range of 0.125–1.25 μM for hypochlorite ($R^2 = 0.985$). The detection limit (LOD) of hypochlorite was calculated to be 0.029 μM at neutral pH. The mPA CNPs were further applied to the cell imaging. The positively charged surface and nanoscale dimension of the mPA CNPs lead to their efficient intracellular delivery. The mPA CNPs were also successfully used for cell imaging and sensitive detection of hypochlorite as well as pH changes in biological systems. Given these desirable performances, the as-synthesized fluorescent mPA CNPs shows great potential as an optical probe for real-time pH and hypochlorite monitoring in living cells.

Keywords: carbon nanomaterials; fluorescence probe; pH sensing; hypochlorite detection; intracellular detection



Citation: Lin, Y.-S.; Chuang, L.-W.; Lin, Y.-F.; Hu, S.-R.; Huang, C.-C.; Huang, Y.-F.; Chang, H.-T. Development of Fluorescent Carbon Nanoparticle-Based Probes for Intracellular pH and Hypochlorite Sensing. *Chemosensors* **2022**, *10*, 64. <https://doi.org/10.3390/chemosensors10020064>

Academic Editor: Camelia Bala

Received: 9 January 2022

Accepted: 30 January 2022

Published: 5 February 2022

Publisher's Note: MDPI stays neutral with regard to jurisdictional claims in published maps and institutional affiliations.



Copyright: © 2022 by the authors. Licensee MDPI, Basel, Switzerland. This article is an open access article distributed under the terms and conditions of the Creative Commons Attribution (CC BY) license (<https://creativecommons.org/licenses/by/4.0/>).

1. Introduction

Many biological functions such as respiratory acidosis [1], lysosomal functions [2], and tumor growth [3] are related to the intracellular pH value. Thus, variation of pH values in biological fluids is usually an index for physiological disorders. For example, the extracellular pH of tumor tissue is lower than that of normal tissue [4]. In addition to pH value, the level and species of reactive oxygen species (ROS) inside cells also need to be carefully monitored because they have been shown to be related to cell signaling like apoptosis and gene expression [5]. Although high concentrations of ROS inside cells could induce carcinogenesis and cell damage, appropriate ROS level is essential for some cellular functions like differentiation. Hypochlorite is one of the important ROS, which is

produced from peroxidation of chloride ions catalyzed by myeloperoxidase (MPO) inside cells [6]. Although hypochlorite plays an important role in the immune system, at high levels it might cause several diseases such as cancer and neuron degeneration [6,7]. Thus, techniques for monitoring of cellular pH value and ROS level are needed.

Many organic molecules and nanomaterials-based fluorescent probes have been shown to be sensitive for monitoring of cellular pH values [8]. Most of the sensing strategies are based on the fact that the fluorescent properties of the probes are pH dependent. For example, we demonstrated a dual emission probe that uses BSA-Au/Ce nanoclusters to monitor cellular pH values, in which the fluorescence intensity of BSA-Ce complex at 410 nm is pH dependent, but that for Au NCs at 650 nm is pH independent [9]. The ratiometric fluorescence approach was validated by measuring the local pH values inside cancer cells. Chen et al. designed another fluorescent probe based on Förster resonance energy transfer (FRET) between a pH-insensitive fluorophore [poly(9,9-dioctylfluorenyl-2,7-diyl), $\lambda_{em} = 439$ nm] and a pH-sensitive fluorescent dye (fluorescein isothiocyanate, $\lambda_{em} = 517$ nm) in the semiconducting polymer dots (Pdots-PPF). Upon a single excitation at 380 nm, the Pdots-PPF exhibit ratiometric pH sensing ability within a wide range of pH value ranging from 3.0 to 8.0 [10]. Recently, fluorescent carbon based-nanoparticles have received great interest due to their low chemical/cytotoxicity, good biocompatibility, multicolor luminescence tunability, and resistance to photobleaching [11–13]. Carbon dots (CDs) prepared by a variety of carbon sources in facile methods have shown significantly improved behaviors and been demonstrated as a suitable candidate for fluorescent pH sensing [13–17].

Relatively, fluorescent probes for determining cellular hypochlorite contents are rare [18–20]. The sensing mechanism behind these probes mainly relies on the strong oxidation property of hypochlorite. For example, Zhong et al. developed an aggregation-induced emission probe based on benzothiazole derivatives (BTD) for hypochlorite detection [21]. The recognition of BTD by hypochlorite involves C=N cleavage and hydrolysis to aldehyde groups. A ratiometric fluorescent probe for hypochlorite was constructed by co-embedding aminocyanine dye and Rhodamine B within a silica nanoparticle to form a FRET pair [22]. It is hypothesized that the nitrogen substitution at the polymethine can be served as a better ROS chemosensor due to its lower oxidation potential. The pioneer work from Yin et al. reported the determination of hypochlorite in a dual-readout mode based on the blue emission CDs with down and up conversion luminescence characteristics [23]. Increasing efforts have been devoted to fabricate CDs with enhanced photoluminescence (PL) properties to detect hypochlorite in real samples [24–27]. It has been found that CDs doped with heteroatoms such as nitrogen or tethered to other functional units can lead to a red-shift in emission and greater reactivity toward hypochlorite [28–31]. It can provide sensitive and selective responses to the hypochlorite in biological systems.

Inspired by the above-mentioned circumstances, we synthesized fluorescent carbon nanoparticles (CNPs) from *m*-phenylenediamine (*m*-PD) and ascorbic acid (AA) through a hydrothermal route to monitor cellular pH and hypochlorite levels. The combination of *m*-PD and AA not only increases the diversity of functional groups, but also brings more active sites, thereby enhancing their responses to target analytes. We investigated several important factors, including molar ratio of *m*-PD/AA and synthesis temperature, which affect the formation of the nanoparticles (mPA CNPs). At the optimal sensing conditions, mPA CNPs showed pH-dependent fluorescence properties over the range of 5.5–8.5, indicating that they are promising for monitoring pH fluctuations in living cells. Under the physiological condition, the probe also showed great sensitivity and selectivity for the quantitation of hypochlorite. We evaluated the possible fluorescence quenching mechanisms of mPA CNPs in response to changes in pH and hypochlorite. The probe was further validated by monitoring cellular pH values and hypochlorite levels, showing their greater potential for cell imaging and real-time sensing.

2. Materials and Methods

2.1. Chemicals and Materials

Ammonium oxalate (>98%), L-(+)-ascorbic acid (AA, $\geq 99.8\%$), monosodium hydrogen phosphate (98%), *m*-phenylenediamine (*m*-PD, >99%), and sodium periodate (99%) were purchased from Acros Organics (Geel, Belgium). Disodium hydrogen phosphate (98%), sodium borohydride ($\geq 98\%$), sodium phosphate (96%), 2'-7'-dichlorofluorescein diacetate (DCFH-DA), Hoechst 33342, potassium nitrite (>96%), potassium dioxide (99%), hydrogen peroxide (36%), iron chloride (>98.0%), dimethyl sulfoxide (DMSO, >99.5%), and sulfuric acid (95–98%) were purchased from Sigma-Aldrich (St. Louis, MO, USA). Sodium hydroxide (pellet, >98%) was purchased from Macron Fine Chemicals (Center Valley, PA, USA). Sodium nitrite was purchased from Thermo Fisher Scientific (Waltham, MA, USA). Sodium hypochlorite (NaClO) (10–12%) was purchased from Aencore (Surrey Hills, Australia). Ultrapure water (18.2 M Ω cm) from a Milli-Q ultrapure system was used in this study.

Superoxide (O_2^-) was generated by dissolving KO_2 in DMSO. Hydroxyl radical ($^{\cdot}OH$) was generated by the Fenton reaction. Typically, hydrogen peroxide (H_2O_2 , 10 eq) was added to $FeCl_2$ in ultrapure water. Peroxynitrite ($ONOO^-$) was prepared by adding 0.6 M KNO_2 , 0.6 M HCl and 0.7 M H_2O_2 to a 3 M NaOH solution at 0 °C. The concentration of $ONOO^-$ was estimated by using the extinction coefficient of 1670 $cm^{-1} M^{-1}$ at 302 nm in 0.1 M aqueous sodium hydroxide solutions. NaClO and H_2O_2 were diluted in ultrapure water.

2.2. Cells Culture

Murine prostate cancer cell line Tramp C1 cells were cultured in Dulbecco's modified Eagle medium (DMEM) containing fetal bovine serum (10%) and penicillin/streptomycin (1%) under a humidified atmosphere of 5% CO_2 in air at 37 °C. The medium was purchased from ThermoFisher Scientific (Waltham, MA, USA).

2.3. Instruments

A monochromatic microplate spectrophotometer (Synerg H1) from Biotek Instruments, (Santa Clara, CA, USA) was used for the fluorescence measurement. A transmission electron microscope (TEM) (H-7100) from Hitachi (Tokyo, Japan) was used to record TEM images of the synthetic products. Field emission transmission electron microscope (FE-TEM) (JEM-2100F) from JEOL (Akishima, Tokyo, Japan) was further used to record their images. Their X-ray photoelectron spectroscopy (XPS) spectra were taken with a system (PHI 5000 VersaProbe III) from ULVAC-PHI (Chigasaki, Kanagawa, Japan). A Fourier transform infrared (FT-IR) spectrophotometer (Varian640-IR) from Varian (Palo Alto, CA, USA) was employed to record their FT-IR spectra. Their ultraviolet-visible (UV-Vis) absorption spectra were taken using a spectrophotometer (Evolution 220; from ThermoFisher Scientific (Waltham, MA, USA)). Their fluorescence spectra were measured using a spectrofluorometer (SF5) from Edinburgh Instruments (Livingston, England). A FluoTime 300 system from PicoQuant (Berlin, Germany) with a diode laser emitting at 375 nm was used as the light source to record the fluorescence decay of mPA CNPs.

2.4. Synthesis of mPA CNPs

A hydrothermal method at various temperatures (170–260 °C; 260 °C is the highest temperature allowed by our heating system) was applied for the synthesis of mPA CNPs from different amounts of *m*-PD (50 mM) and AA (25–100 mM). Based on the yield, stability, and optical properties of the product, reaction temperature at 260 °C for 2 h, 50 mM of *m*-PD, 50 mM of AA, and solution pH of 4.0 were selected. In brief, *m*-PD (54 mg, 0.5 mmol) and AA (88 mg, 0.5 mmol) were dissolved in 10 mL ultrapure water (adjusted with 1 M HCl to pH 4.0), which were then poured into a 50 mL Teflon-lined stainless steel autoclave. After reaction at 260 °C for 2 h, the mixture was cooled to ambient temperature before conducting centrifugation at 3000 g under ambient temperature for 10 min. The pellet

was discarded, and the supernatant (c.a. 4 mL) was subjected to dialysis with a dialysis bag (100–500 Da cut-off) against ultrapure water (1 L) for 24 h. Subsequently, the product (mPA CNPs) was collected. We also noticed that no changes in appearance, UV-Vis, and FL spectra were observed by simply mixing *m*-PD (54 mg) and AA (88 mg) at pH 4 for 2 h without heating. As a control, *m*-PD (54 mg) or AA (88 mg) were dissolved in 10 mL of ultrapure water and subjected to the same hydrothermal synthesis and purification procedures. The purified products were then dispersed in ultrapure water before use.

2.5. Determination of Fluorescence Quantum Yield and Lifetime

The quantum yield (QY) of mPA CNPs was determined by a relative measurement method. Quinine sulfate (QY = 0.53 in 0.05 M sulfuric acid, $\lambda_{\text{ex}} = 385 \text{ nm}$) was chosen as the reference sample. The QY was calculated using the equation:

$$\phi = \phi' \times \frac{A'}{I'} \times \frac{I}{A} \times \frac{n^2}{n'^2}$$

where ϕ , A , and I are the QY, absorbance, and the integrated fluorescence emission intensity of the testing sample, respectively, and n is the refractive index. The prime symbol (') is used to denote the parameters of the selected reference. The optical density of a series solutions of the testing and reference samples was adjusted to the range of 0–0.1. The fluorescence spectra were measured and the fluorescence intensity of the emitted light was integrated. The QY of the testing sample can be determined by comparing the integrated fluorescence intensity versus absorbance.

The fluorescence decay of mPA CNPs was fitted with a single-exponential decay function:

$$I_t = I_0 \exp\left(\frac{-t}{\tau}\right)$$

where, I_0 and I_t are the intensity at time zero and a specific time t , respectively. τ is fluorescence lifetime defined as the time for the intensity to drop to 37%. The sample concentration was $1.0 \mu\text{g mL}^{-1}$. The relationship between the rate constants (radiative rate, k_r ; non-radiative rate, k_{nr}), fluorescence lifetime (τ), and QY (ϕ) can be described as the following equations:

$$\tau = \frac{1}{k_r + k_{nr}}, \phi = \frac{k_r}{k_r + k_{nr}}$$

The radiative rate and non-radiative rate can be calculated as:

$$\frac{\phi}{\tau} = \frac{k_r}{k_r + k_{nr}} \times (k_r + k_{nr}) = k_r, \frac{1}{\tau} - k_r = k_{nr}$$

2.6. pH Sensing Based on mPA CNPs

To study the pH responsiveness of mPA CNPs, various mPA CNPs ($1 \mu\text{g mL}^{-1}$) solutions were prepared by mixing mPA CNPs ($10 \mu\text{g mL}^{-1}$, $50 \mu\text{L}$), ultrapure water ($400 \mu\text{L}$), and phosphate buffer (200 mM , $50 \mu\text{L}$) with different pH values (pH 3.0–11.0) for 10 min. Their UV-Vis and fluorescence spectra were then recorded. To investigate the reversibility of pH response of mPA CNPs, the solutions containing 5-fold concentration of mPA CNPs at pH 3.0 were prepared in a similar manner, and then adjusted to various pH values by adding 0.1 M NaOH or HCl. To record the fluorescence microscopic images of mPA CNPs, mPA CNPs ($100 \mu\text{g mL}^{-1}$, $10 \mu\text{L}$) prepared at various pH values were applied separately to microslides and each slide was covered with a glass.

2.7. Detection of ROS and Anti-Oxidants Based on mPA CNPs

To determine the sensitivity of the assay for hypochlorite, various solutions were prepared by mixing mPA CNPs ($5 \mu\text{g mL}^{-1}$, $50 \mu\text{L}$), phosphate buffer (200 mM , pH 7.4, $50 \mu\text{L}$), and solutions ($400 \mu\text{L}$) containing different concentrations of sodium hypochlorite. The final concentration of hypochlorite is in the range of 0.125–1.25 μM . After equilibration

at 25 °C for 1 h, the solutions were subjected to fluorescence measurement at 500 nm when excited at 400 nm.

Various solutions were separately prepared by mixing mPA CNPs (50 µg mL⁻¹, 50 µL), ultrapure water (350 µL), phosphate buffer (200 mM, pH 7.4, 50 µL), and tested substrates [1 mM of H₂O₂, O₂⁻, ·OH, NaNO₂, (NH₄)₂C₂O₄, and NaBH₄, 50 µL; 100 µM of ONOO⁻ and NaClO, 50 µL]. After shaking at 160 rpm for 30 min at 25 °C, their fluorescence spectra were recorded under 400 nm excitation.

2.8. *In Vitro* Biocompatibility Assessment

The cell viability was evaluated by conducting the Alamar blue assay. Tramp C1 cells seeded at a density of 8000 cells per 96-well plate were incubated overnight in DMEM (200 µL) for cell adhesion. Then, the cells were treated with various concentrations of mPA CNPs (0–20 µg mL⁻¹) for 2 h. The treated cells were then washed with phosphate buffer saline (PBS) and incubated with refreshed DMEM for 24 h. The next day, the medium was removed and replaced with 100 µL of diluted Alamar Blue agent (diluted 10 times with DMEM) for 2 h. The fluorescence intensity at 595 nm was measured under the excitation at a wavelength of 545 nm.

2.9. *In Vitro* pH Detection

To study the pH response of mPA CNPs in living cells, Tramp C1 cells seeded at a density of 1.0×10^5 cells per 24-well plate (with a round-shaped glass inside each well) were incubated overnight in DMEM (500 µL) for cells adhesion. Then, the medium was replaced with PBS of different pH values (pH 5.4, 6.4, 7.4, and 8.4) before adding mPA CNPs solutions (50 µg mL⁻¹, 50 µL). After 2 h incubation, the medium was replaced with PBS (500 µL). The cells were then treated with Hoechst 33342 (5 µg mL⁻¹) for 10 min, followed by multiple washes with PBS. A paraformaldehyde solution (PFA, 500 µL) was added to fix the cells for 15 min. Finally, the PFA solution was removed and the cells were washed with PBS (500 µL). The glass in each well was then taken out, dried, and placed on a microslide containing 10 µL of mounting medium. Fluorescence cell images were captured with the fluorescence microscope (excitation/emission filters: 470–490 nm band pass/520 nm long pass).

For the flow cytometry measurement, the treated cells were washed with PBS and detached from the plate by trypsin (0.25%, 200 µL). The medium (400 µL) were then added to inactivate trypsin. The cell pellet was collected by centrifugation at $500 \times g$ for 5 min and subjected to flow cytometry analysis.

2.10. *In Vitro* Hypochlorite Detection

Similar to the above method, Tramp C1 cells were seeded at a density of 1.0×10^5 cells per 24-well plate and incubated overnight for cells adhesion. Afterwards, the medium with mPA CNPs solution (5 µg mL⁻¹) was replaced for 2 h incubation. The treated cells were then washed with PBS and incubated with PBS in the absence and presence of NaClO (10 µM). Fluorescence images were taken at different time spans from 0 to 30 min. Trypsinization was also performed to collect cells under different treatments, followed by flow cytometry analysis.

3. Results and Discussion

3.1. Characterization of mPA CNPs

We found that the yield, absorbance, and the fluorescence intensity of mPA CNPs increase upon elevating the hydrothermal temperature from 170 to 260 °C. For example, the fluorescence intensity ratio of mPA CNPs obtained at 170, 200, 230, and 260 °C is 1:2.0:4.4:6.2. We noticed that temperature did not play a significant role in affecting their characteristic features of absorption and fluorescence spectra. For this reason, only the mPA CNPs prepared at 260 °C for 2 h were subjected to further characterization and used to develop sensitive probes. In addition, the products prepared separately from

m-PD and AA have also been characterized to support the advantages of mPA CNPs over these two products.

The TEM image depicted in Figure 1A shows that mPA CNPs have spherical structures, with an average size of 232 ± 53 nm (50 counts). The surfaces of mPA CNPs are rough as shown in the inset of Figure 1A. When *m*-PD is the only precursor (Figure S1A), *m*-PD CDs with an average size of 7.5 ± 1.4 nm and interlayer spacing of 0.31 nm were obtained, corresponding to the (002) plane lattice of graphite [32]. According to the literature, the *m*-PD CDs were formed through processes including oxidation, polymerization, carbonization, and passivation [33]. When AA was used as the precursor, irregular and flake-shaped materials were obtained as shown in Figure S1B. The three TEM images suggest that the AA should play a certain role in the formation of large-scale mPA CNPs. It has been reported that a fluorescent material can be produced through the condensation reaction between *m*-PD and AA at ambient condition [34]. The formation of large mPA CNPs may be caused by the subsequent condensation during the heating process. It is also important to highlight that lattice fringes were only observed in the *m*-PD CDs sample. This indicates that with the supply of AA, the graphitization of *m*-PD tends to be retarded, resulting in CNPs consisting of polymer chains with a slight degree of carbonization. In this study, we also found that the molar ratio of *m*-PD/AA only affects the absorbance and fluorescence intensity. The ratio of fluorescence intensities at 500 nm of the products prepared with the molar ratio of *m*-PD/AA of 0.5, 1, and 2 is 0.9:1:0.7. Figure 1B shows the absorption spectrum of mPA CNPs. There is a sharp peak at 242 nm and a broad band over 320 to 450 nm, which separately correspond to the π - π^* transition in benzenoid rings and the higher conjugated polymer chains [35]. The fluorescence spectra of mPA CNPs depicted in Figure 1C exhibit both excitation-dependent/independent emission properties, with the strongest PL intensity at 500 nm when excited at the wavelength of 400 nm. The fluorescence QY, lifetime, radiative rate, and non-radiative rate are approximately 10%, 7.91 ns, 1.26×10^7 s⁻¹, and 1.14×10^8 s⁻¹, respectively. The fluorescent properties are similar to those of CDs reported in the literature [36]. In contrast, *m*-PD CDs like most CDs show excitation-dependent emission properties as shown in the inset of Figure S1C [11–14], with the strongest emission intensity in the blue region. Figure S1C shows a sharp absorption peak at 290 nm and a broadband at 320–350 nm of *m*-PD CDs, corresponding to the π - π^* transition of aromatic C=C bonds and n- π^* transition of C=O and C=N bonds at the edge of the carbon lattice, respectively [37]. As compared to the fully carbonized *m*-PD CDs, the bright green emission originated from mPA CNPs could be attributed to the crosstalk of multiple luminescence centers, including molecular-state, crosslink-enhanced-emission-effect-related state, sp² subdomains (carbon core state), and surface state [38]. The product obtained from AA only emits weakly at 395 nm when excited at 255 nm, so we will not discuss it hereafter.

The XPS spectra displayed in Figure S2 indicate that mPA CNPs and *m*-PD CDs are predominantly composed of carbon, nitrogen, oxygen. The high-resolution C_{1s} spectrum is deconvoluted into five individual component peaks, corresponding to -C-C/-C=C (284.6 eV), -C-N (285.3 eV), -C-O (286.0 eV), -C=O/-C=N (288.1 eV), and -COO (289.0 eV), respectively [39,40]. The signal of C-C/C=C in mPA CNPs is lower, but the sum of C-O, C=O, and COO peak intensities is higher than *m*-PD CDs. This result is consistent with our findings shown in Figure 1A and Figure S1A, indicating that the engagement of AA leads to the successful incorporation of oxygen-containing residues into the polymer chains/carbon hybrid structures. The detection of a stronger -C=O (531.8 eV) signal over -C-O (532.8 eV) in mPA CNPs also confirms that they exhibit a higher oxidation state than *m*-PD CDs due to AA [41,42]. The N_{1s} XPS peaks at 399, 399.9, and 401.1 eV were assigned to pyridinic N, amino N and the sum of graphitic N and protonated amino N, respectively [43,44]. The aliphatic-to-aromatic N ratio signal detected in mPA CNPs is stronger than *m*-PD CDs, indicating that there are abundant amino groups decorated on the surface/polymer chains.

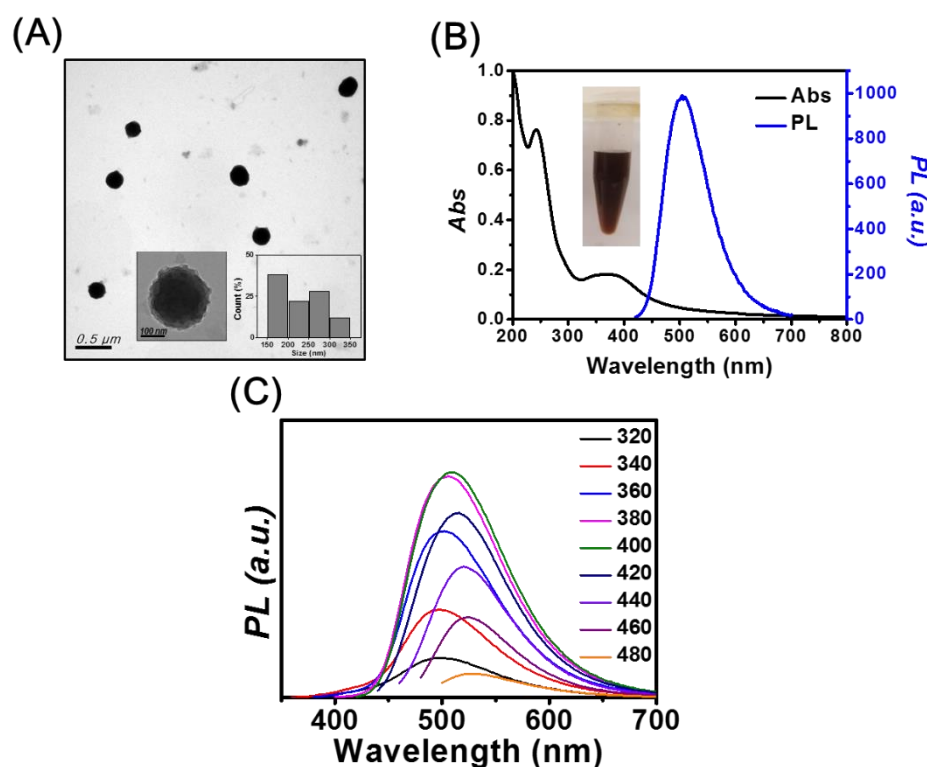


Figure 1. (A) TEM image of mPA CNPs. Inset: high resolution TEM image and size distribution analysis. (B) UV-Vis absorption and fluorescence spectra of *m*-PD CDs excited at 400 nm. Inset: photograph of 1 mg mL⁻¹ mPA CNPs solution. (C) Fluorescence spectra of mPA CNPs in aqueous solution as a function of excitation wavelength from 320 to 480 nm.

For the FT-IR spectra of mPA CNPs and *m*-PD CDs depicted in Figure S3, the peaks observed at 3408 and 3313 cm⁻¹, the broad band around 3212 cm⁻¹, and the peak at 3035 cm⁻¹ were attributed to the stretching vibrations of N–H, O–H, and aromatic C–H, respectively [45]. The intense signal centered at around 1632 cm⁻¹ conveyed signals from quinoid imine stretching, –C=C– ring stretching and –NH₂ bending, and the peaks registered at 1500 and 1334 cm⁻¹ were separately assigned to the C=C and C–N stretching vibrations of benzenoid amine [46,47]. The characteristic peak of C=O stretching at 1701 cm⁻¹ indicates the introduction of AA residues in mPA CNPs [48]. The spectral features of mPA CNPs are comparatively more apparent than those of *m*-PD CDs, further confirming the greater retention of pyrolytic *m*-PD/AA polymers.

3.2. pH Sensing Based on mPA CNPs

As illustrated in Figure 2A, the PL intensity of mPA CNPs (1.0 µg mL⁻¹) at 500 nm decreases upon increasing pH values from 3.0 to 11.0. The UV-Vis spectra displayed in the inset of Figure 2A also show blue shifts of the peaks from 260 to 240 nm and 400 to 350 nm upon increasing the pH value. Figure 2B shows that the fluorescence intensity of mPA CNPs exhibit a linear response to pH over the range of 5.5 to 8.5 ($R^2 = 0.989$), revealing their potential for pH sensing of biological samples. It is expected that the pH responsiveness of mPA CNPs is resulted from the protonation/deprotonation of the amino and carboxyl groups, respectively [49,50]. As depicted in Table S1, the zeta potential of mPA CNPs becomes less positive as pH increases, which supports our hypothesis. Meanwhile, mPA CNPs undergo aggregation, as demonstrated in the fluorescence microscopic images in Figure 2C and the corresponding hydrodynamic sizes detected by dynamic light scattering were 352 ± 15, 803 ± 104, and 1157 ± 224 nm, at pH values of 3.0, 7.0, and 11.0, respectively. Due to the aggregation behavior, non-radiative energy transfer such as photoinduced electron transfer (PET) can readily occur through the close proximity of neighboring amine

groups [51,52]. The fluorescence lifetimes of mPA CNPs were investigated and the average values at pH 3.0 (8.19 ns), 7.0 (7.91 ns), and 11.0 (7.02 ns) were obtained from the fluorescence decay curves in Figure S4. The reduced lifetime indicates that the mPA CNPs undergoes an ultra-fast electron transfer process when excited at higher pH values. This combined dynamic and static quenching mechanism based on the fluorescence quenching of mPA CNPs can be adopted to develop high-efficiency pH sensors. We further investigated the reversibility of the pH response of mPA CNPs by alternately changing the pH value of the solution from 3.0 to 11.0 in three consecutive cycles (3.0-11.0-3.0). The results shown in Figure 2D demonstrates that the fluorescence intensity of mPA CNPs is reversible under cycling various pH. In addition, the inset photograph also shows that the color of the solution becomes lighter, but cloudy under alkaline conditions.

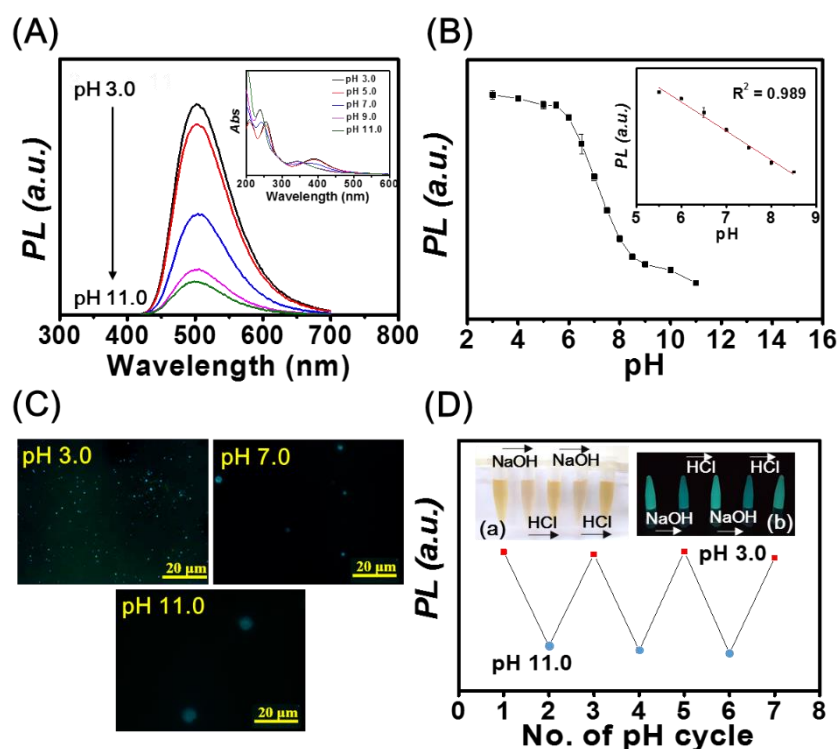


Figure 2. (A) Fluorescence spectra of mPA CNPs ($1 \mu\text{g mL}^{-1}$) at pH values of 3.0, 5.0, 7.0, 9.0, and 11.0. Inset: Corresponding UV-Vis spectra of mPA CNPs ($1 \mu\text{g mL}^{-1}$). (B) Plot of the fluorescence intensity at 500 nm versus pH values. (C) Fluorescence microscopic images of mPA CNPs at pH 3.0, 7.0, and 11.0. (D) The fluorescence intensity of mPA CNPs at 500 nm cycled between pH 3.0 and 11.0. Inset: Corresponding photographs under (a) white light and (b) UV light. The pH of the mPA CNPs solution is switched back and forth between 3.0 and 11.0 by using 0.1 M HCl or NaOH solutions, respectively. Excitation and emission wavelengths are 400 and 500 nm, respectively.

Encouraged by the results mentioned above, mPA CNPs were applied for intracellular pH monitoring. As displayed in Figure 3, the fluorescence intensity of mPA CNPs in Tramp C1 cells progressively decreased with the pH increasing from 5.4 to 8.4. The average intensity of fluorescent from each event was further quantified using the flow cytometry (Figure S5), and the fluorescence of mPA CNPs is pH-dependent in living cells, corresponding to that in the fluorescence spectra (Figure 2A,B). Compared with other CDs previously reported (Table S2) [16,39,49,50,53–55], mPA CNPs are effective for cell staining as satisfactory and reliable cell images can be achieved with a relatively reduced dose ($5 \mu\text{g mL}^{-1}$ for 2 h). It should also be noted that mPA CNPs exhibit eligible biocompatibility. It can be found that under the same cultivation conditions, more than 80 % of cells survived as the dose of mPA CNPs is less than $20 \mu\text{g mL}^{-1}$ (Figure S6). Taken together, mPA CNPs are competent for intracellular pH sensing.

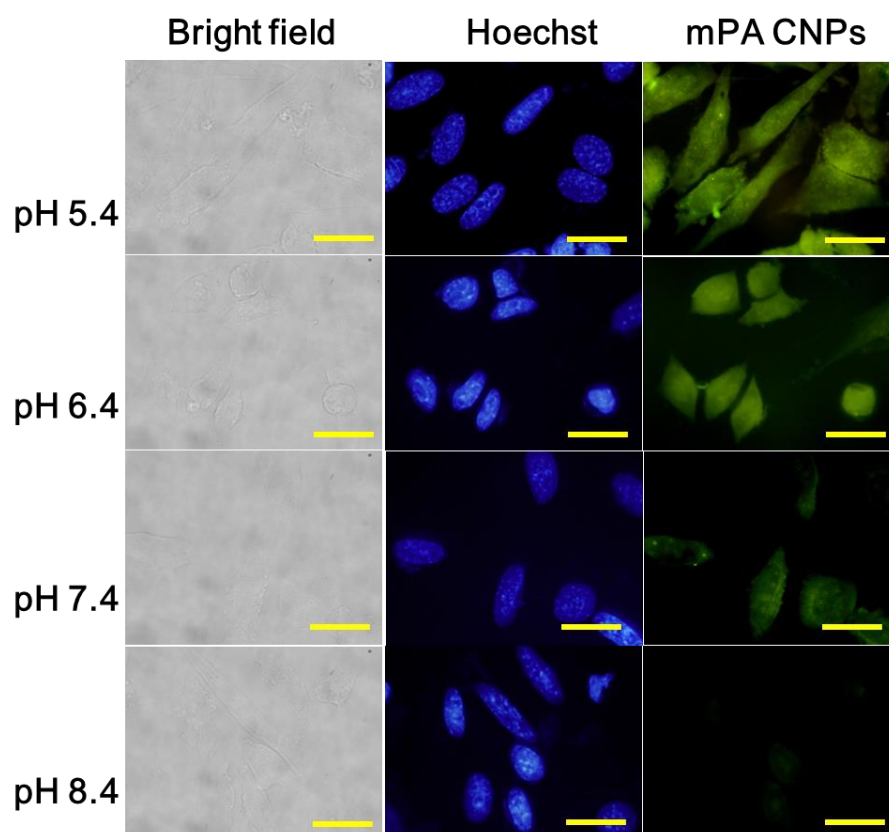


Figure 3. Fluorescence microscopic images of Tramp C1 cells stained with mPA CNPs ($5 \mu\text{g mL}^{-1}$) were exposed to various PBS solutions at pH 5.4, 6.4, 7.4, and 8.4 for 2 h. From left to right were different channels: bright field, blue channel ($\lambda_{\text{ex}} = 350\text{--}380 \text{ nm}$, $\lambda_{\text{em}} = 420 \text{ nm}$) and green channel ($\lambda_{\text{ex}} = 470\text{--}490 \text{ nm}$, $\lambda_{\text{em}} = 520 \text{ nm}$). The scale bar denotes $20 \mu\text{m}$.

3.3. Hypochlorite Sensing Based on mPA CNPs

Hypochlorite can induce the fluorescence quenching of mPA CNPs ($0.5 \mu\text{g mL}^{-1}$) at 500 nm , and the intensity exhibits a linear relationship ($R^2 = 0.985$) with the concentration in the range of $0.125\text{--}1.25 \mu\text{M}$ in phosphate buffer at pH 7.4 (Figure 4A). The limit of detection (LOD) was estimated to be $0.029 \mu\text{M}$ based on the signal-to-noise ratio of three. Table S3 shows that mPA CNPs provides comparable sensitivity to hypochlorite when compared to the other reported methods based on CDs [24–27,29,31,56]. It is well accepted that the surface functional groups such as aromatic amines possess a high tendency to oxidize when hypochlorite is introduced [28,31]. In this sensing process, static fluorescence quenching occurs due to the generation of less or non-fluorescent ground state complexes. In view of this, the FT-IR spectra of mPA CNPs versus hypochlorite was explored. As depicted in Figure S7, the characteristic absorption peaks at 3200 and 1334 cm^{-1} corresponding to N–H and C–N stretching vibrations were reduced, while the peak at 1632 cm^{-1} increased due to the appearance of more quinoid imine after the introduction of hypochlorite. The selectivity of mPA CNPs ($5 \mu\text{g mL}^{-1}$) toward hypochlorite (NaClO) over common ROS (H_2O_2 , O_2^- , ONOO^- , OH) and various antioxidants [NaNO_2 , $(\text{NH}_4)_2\text{C}_2\text{O}_4$, and NaBH_4] was further investigated. Figure 4B shows that hypochlorite ($10 \mu\text{M}$) caused significant fluorescence quenching of mPA CNPs, while the effects of other substances ($100 \mu\text{M}$) were almost negligible. Only a slight fluorescence quenching of mPA CNPs was found in the presence of OH radical ($100 \mu\text{M}$). From Table S4, it can be observed that the one electron redox potential of NaClO (1.49 eV) is the highest except for OH radical (2.33 eV) [57–59]. In addition, the negatively charged nature of hypochlorite also makes them readily accessible to the mPA CNPs surface via electrostatic interactions, resulting in a superior propensity for oxidation. The performance of mPA CNPs on hypochlorite detection was further compared

with DCFH-DA, which is a commercial dye commonly used to detect various ROS. As Figure 4C displayed, mPA CNP provides a more selective response to hypochlorite than DCFH-DA. These findings confirm the promising bioapplicability of mPA CNP in the detection of hypochlorite in living cells.

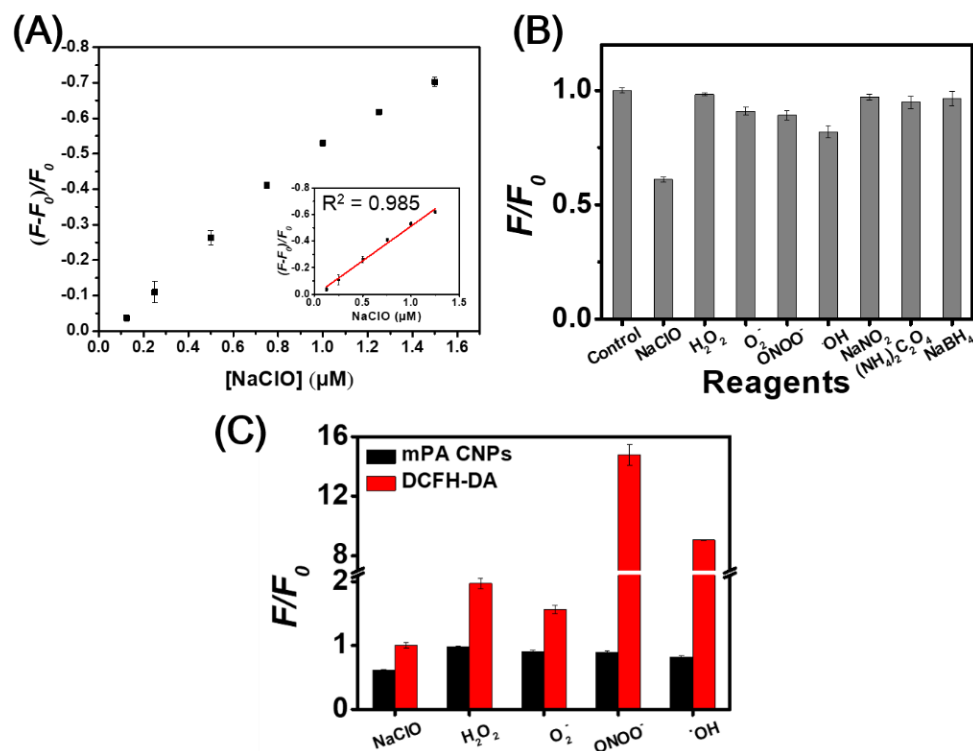


Figure 4. (A) Plot of the fluorescence reduction of mPA CNPs versus hypochlorite concentration. The linear relationship between $(F-F_0)/F_0$ and NaClO concentration ranges from 0.125 to 1.5 μM . F_0 and F denote the fluorescence intensities of mPA CNPs at 500 nm in the absence and presence of hypochlorite. Excitation wavelength is 400 nm. (B) Effects of potential interferences on fluorescence intensities of mPA CNPs ($5 \mu\text{g mL}^{-1}$) at 500 nm in 20 mM phosphate buffer (pH 7.4). The concentrations of NaClO and ONOO $^-$ are both 10 μM and the concentrations of H_2O_2 , O_2^- , OH, NaNO_2 , $(\text{NH}_4)_2\text{C}_2\text{O}_4$, and NaBH_4 are all 100 μM . (C) Fluorescence intensity changes of mPA CNPs ($5 \mu\text{g mL}^{-1}$) or DCFH-DA (25 μM) in 20 mM phosphate buffer (pH 7.4) toward various ROS and ONOO $^-$. F_0 and F denote separately the fluorescence intensities of respective probe in the absence and presence of different analytes. DCF fluorescence is detected by using excitation and emission wavelengths of 485 and 535 nm, respectively.

Subsequently, mPA CNPs was employed as a fluorescent probe for specific detection of hypochlorite in Tramp C1 cells. As shown in Figure 5, cells emit green fluorescence when they were stained with $5 \mu\text{g mL}^{-1}$ of mPA CNPs for 2 h. After the introduction of NaClO (10 μM), the fluorescence intensity decreased gradually and demonstrates an effective diminish after 30 min. In addition, the fluorescence intensity of mPA CNPs after 30 min of stimulus was also detected by flow cytometry (Figure S8). The bar graph shows that the fluorescence of mPA CNPs was reduced by approximately 25% after hypochlorite treatment. On the contrary, after co-treatment with *N*-acetylcysteine (NAC, 10 mM), an ROS scavenger, no fluorescence quenching of mPA CNPs was detected since the hypochlorite-mediated oxidation was inhibited. Therefore, mPA CNPs developed herein can be regarded as a potential probe for real-time detecting hypochlorite changes in cells stimulated by different pharmaceuticals.

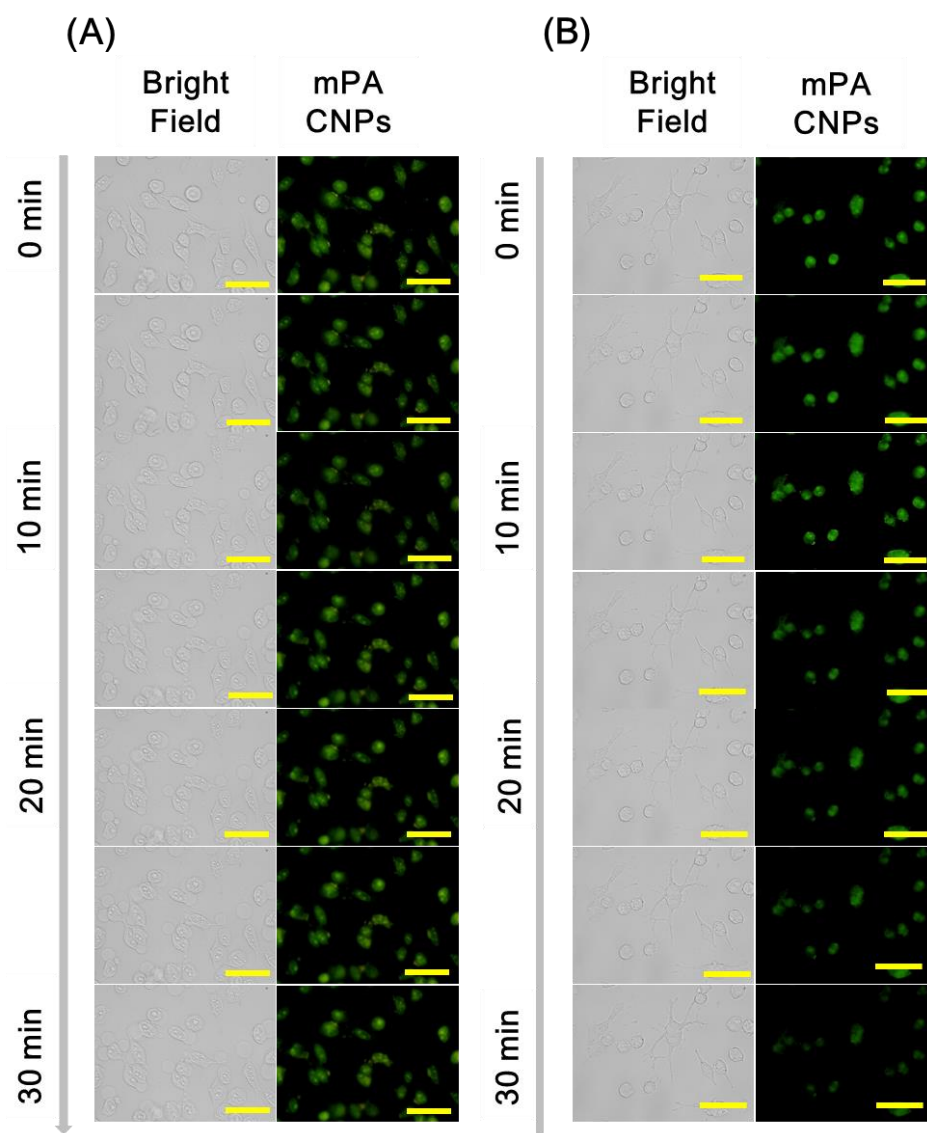


Figure 5. Fluorescence microscopic images of Tramp C1 cells incubated with mPA CNPs ($5 \mu\text{g mL}^{-1}$) in DMEM medium (pH 7.4) for 2 h. Afterwards, the stained cells were stimulated with PBS in (A) the absence of and (B) the presence of $10 \mu\text{M NaClO}$. Fluorescence images were collected at different time spans from 0 to 30 min. From left to right are different channels: bright field and green channel ($\lambda_{\text{ex}} = 470\text{--}490 \text{ nm}$, $\lambda_{\text{em}} = 520 \text{ nm}$). The scale bar denotes $32 \mu\text{m}$.

4. Conclusions

In the study, we developed a novel type of fluorescent probe, mPA CNPs with pH sensing and hypochlorite detection capabilities. Through a one-pot hydrothermal process using two different carbon sources, green emission fluorescent CNPs with a QY of 10% were generated. Due to the existence of effective functional groups, the as-prepared mPA CNPs exhibited favorable responsiveness toward pH and hypochlorite. In response to higher pH values, the fluorescence of mPA CNPs decreased through a combination of static and dynamic quenching mechanisms due to the deprotonation of amino groups. In addition, hypochlorite with high oxidation potential for aromatic amines was capable of reducing the PL of mPA CNPs based on static quenching. The mPA CNPs have been successfully applied to cell imaging owing to their high efficiency of cell uptake and good biocompatibility. With the pH-sensitive response in the range of 5.5–8.5 and high selectively to hypochlorite among other interfering analytes, mPA CNPs further demonstrated their

promising potential for fluorescence sensing of pH values and hypochlorite in Tramp C1 living cells.

Supplementary Materials: The following supporting information can be downloaded at: <https://www.mdpi.com/article/10.3390/chemosensors10020064/s1>, Figure S1: TEM image, UV-Vis and fluorescence spectra of *m*-PD CDs, Figure S2: XPS spectra of *m*-PD CDs and mPA CNPs, Figure S3: FT-IR spectra of mPA CNPs and *m*-PD CDs, Figure S4: Fluorescence decay curves of mPA CNPs at various pH, Figure S5: Flow cytometry analysis of Tramp C1 cells treated with mPA CNPs at various pH, Figure S6: Cell viability for Tramp C1 cells in the presence of mPA CNPs, Figure S7: FT-IR spectra of mPA CNPs in the absence and presence of NaClO, Figure S8: Flow cytometry analysis of Tramp C1 cells stained by mPA CNPs incubated with NaClO or NaClO/NAC, Table S1: Zeta potentials of mPA CNPs at various pH values, Table S2: Comparison of the in vitro fluorescence behavior of mPA CNPs with other CD-based pH sensors, Table S3: Comparison of the fluorescence behavior of mPA CNPs with other CD-based hypochlorite sensors, Table S4: One electron redox potential of ROS and antioxidants.

Author Contributions: Conceptualization, H.-T.C. and Y.-F.H.; Methodology, L.-W.C. and Y.-S.L.; Software, Y.-S.L.; Validation, Y.-S.L., Y.-F.L. and S.-R.H.; Writing—original draft preparation, L.-W.C. and Y.-S.L.; Writing—review and editing, Y.-S.L., C.-C.H., Y.-F.H. and H.-T.C.; Supervision, C.-C.H. and H.-T.C.; Project administration, H.-T.C. All authors have read and agreed to the published version of the manuscript.

Funding: The Ministry of Science and Technology supported this study, Taiwan, under contracts 110-2113-M-002-005-MY3, 110-2622-M-002-001, and 108-2638-M-002-001-MY2.

Data Availability Statement: The data presented in this study are available from the Supplementary Materials section.

Conflicts of Interest: The authors declare no conflict of interest.

References

1. Arieff, A.I.; Kerian, A.; Massry, S.G.; DeLima, J. Intracellular pH of brain: Alterations in acute respiratory acidosis and alkalosis. *Am. J. Physiol.* **1976**, *230*, 804–812. [[CrossRef](#)] [[PubMed](#)]
2. Tapper, H.; Sundler, R. Role of lysosomal and cytosolic pH in the regulation of macrophage lysosomal enzyme secretion. *Biochem. J.* **1990**, *272*, 407–414. [[CrossRef](#)] [[PubMed](#)]
3. Persi, E.; Duran-Frigola, M.; Damaghi, M.; Roush, W.R.; Aloy, P.; Cleveland, J.L.; Gillies, R.J.; Ruppin, E. Systems analysis of intracellular pH vulnerabilities for cancer therapy. *Nat. Commun.* **2018**, *9*, 2997. [[CrossRef](#)] [[PubMed](#)]
4. Kato, Y.; Ozawa, S.; Miyamoto, C.; Maehata, Y.; Suzuki, A.; Maeda, T.; Baba, Y. Acidic extracellular microenvironment and cancer. *Cancer Cell Int.* **2013**, *13*, 89. [[CrossRef](#)]
5. Weinberg, F.; Ramnath, N.; Nagrath, D. Reactive oxygen species in the tumor microenvironment: An overview. *Cancers* **2019**, *11*, 1191. [[CrossRef](#)]
6. Chen, P.; Zheng, Z.; Zhu, Y.; Dong, Y.; Wang, F.; Liang, G. Bioluminescent turn-on probe for sensing hypochlorite in vitro and in tumors. *Anal. Chem.* **2017**, *89*, 5693–5696. [[CrossRef](#)]
7. Nussold, C.; Kollroser, M.; Kofeler, H.; Rechberger, G.; Reicher, H.; Ullen, A.; Bernhart, E.; Wärtl, S.; Kratzer, I.; Hermetter, A.; et al. Hypochlorite modification of sphingomyelin generates chlorinated lipid species that induce apoptosis and proteome alterations in dopaminergic PC12 neurons in vitro. *Free Radic. Biol. Med.* **2010**, *48*, 1588–1600. [[CrossRef](#)]
8. Hou, J.T.; Ren, W.X.; Li, K.; Seo, J.; Sharma, A.; Yu, X.Q.; Kim, J.S. Fluorescent bioimaging of pH: From design to applications. *Chem. Soc. Rev.* **2017**, *46*, 2076–2090. [[CrossRef](#)]
9. Chen, Y.-N.; Chen, P.-C.; Wang, C.-W.; Lin, Y.-S.; Ou, C.-M.; Ho, L.-C.; Chang, H.-T. One-pot synthesis of fluorescent BSA-Ce/Au nanoclusters as ratiometric pH probes. *Chem. Commun.* **2014**, *50*, 8571–8574. [[CrossRef](#)]
10. Chen, P.; Ilyas, I.; He, S.; Xing, Y.; Jin, Z.; Huang, C. Ratiometric pH sensing and imaging in living cells with dual-emission semiconductor polymer dots. *Molecules* **2019**, *24*, 2923. [[CrossRef](#)]
11. Chu, H.-W.; Unnikrishnan, B.; Anand, A.; Lin, Y.-W.; Huang, C.-C. Carbon quantum dots for the detection of antibiotics and pesticides. *J. Food Drug Anal.* **2020**, *28*, 539–557. [[CrossRef](#)]
12. Han, A.; Hao, S.; Yang, Y.; Li, X.; Luo, X.; Fang, G.; Liu, J.; Wang, S. Perspective on recent developments of nanomaterial based fluorescent sensors: Applications in safety and quality control of food and beverages. *J. Food Drug Anal.* **2020**, *28*, 486–507. [[CrossRef](#)]
13. Xu, D.; Lin, Q.; Chang, H.-T. Recent advances and sensing applications of carbon dots. *Small Methods* **2020**, *4*, 1900387. [[CrossRef](#)]
14. Ehtesabi, H.; Hallaji, Z.; Najafi Nobar, S.; Bagheri, Z. Carbon dots with pH-responsive fluorescence: A review on synthesis and cell biological applications. *Microchim. Acta* **2020**, *187*, 150. [[CrossRef](#)]

15. Song, W.; Duan, W.; Liu, Y.; Ye, Z.; Chen, Y.; Chen, H.; Qi, S.; Wu, J.; Liu, D.; Xiao, L.; et al. Ratiometric detection of intracellular lysine and pH with one-pot synthesized dual emissive carbon dots. *Anal. Chem.* **2017**, *89*, 13626–13633. [[CrossRef](#)]
16. Ye, X.; Xiang, Y.; Wang, Q.; Li, Z.; Liu, Z. A red emissive two-photon fluorescence probe based on carbon dots for intracellular pH detection. *Small* **2019**, *15*, 1901673. [[CrossRef](#)]
17. Zhang, M.; Su, R.; Zhong, J.; Fei, L.; Cai, W.; Guan, Q.; Li, W.; Li, N.; Chen, Y.; Cai, L.; et al. Red/orange dual-emissive carbon dots for pH sensing and cell imaging. *Nano Res.* **2019**, *12*, 815–821. [[CrossRef](#)]
18. Li, D.; Feng, Y.; Lin, J.; Chen, M.; Wang, S.; Wang, X.; Sheng, H.; Shao, Z.; Zhu, M.; Meng, X. A mitochondria-targeted two-photon fluorescent probe for highly selective and rapid detection of hypochlorite and its bio-imaging in living cells. *Sens. Actuators B Chem.* **2016**, *222*, 483–491. [[CrossRef](#)]
19. Vedamalai, M.; Kedaria, D.; Vasita, R.; Gupta, I. Oxidation of phenothiazine based fluorescent probe for hypochlorite and its application to live cell imaging. *Sens. Actuators B Chem.* **2018**, *263*, 137–142. [[CrossRef](#)]
20. Feng, Y.; Li, S.; Li, D.; Wang, Q.; Ning, P.; Chen, M.; Tian, X.; Wang, X. Rational design of a diaminomaleonitrile-based mitochondria—targeted two-photon fluorescent probe for hypochlorite in vivo: Solvent-independent and high selectivity over Cu^{2+} . *Sens. Actuators B Chem.* **2018**, *254*, 282–290. [[CrossRef](#)]
21. Zhong, X.; Yang, Q.; Chen, Y.; Jiang, Y.; Dai, Z. Aggregation-induced fluorescence probe for hypochlorite imaging in mitochondria of living cells and zebrafish. *J. Mater. Chem. B* **2020**, *8*, 7375–7381. [[CrossRef](#)] [[PubMed](#)]
22. Chen, G.; Song, F.; Wang, J.; Sun, S.; Fan, J.; Qiang, X.; Wang, X.; Dou, B.; Peng, X. FRET spectral unmixing: A ratiometric fluorescent nanoprobe for hypochlorite. *Chem. Commun.* **2012**, *48*, 2949–2951. [[CrossRef](#)] [[PubMed](#)]
23. Yin, B.; Deng, J.; Peng, X.; Long, Q.; Zhao, J.; Lu, Q.; Chen, Q.; Li, H.; Tang, H.; Zhang, Y.; et al. Green synthesis of carbon dots with down- and up-conversion fluorescent properties for sensitive detection of hypochlorite with a dual-readout assay. *Analyst* **2013**, *138*, 6551–6557. [[CrossRef](#)]
24. Hu, Y.; Yang, J.; Jia, L.; Yu, J.-S. Ethanol in aqueous hydrogen peroxide solution: Hydrothermal synthesis of highly photoluminescent carbon dots as multifunctional nanosensors. *Carbon* **2015**, *93*, 999–1007. [[CrossRef](#)]
25. Simoes, E.F.C.; Silva, L.P.; Silva, J.C.G.E.; Leitao, J.M.M. Hypochlorite fluorescence sensing by phenylboronic acid-alizarin adduct based carbon dots. *Talanta* **2020**, *208*, 120447. [[CrossRef](#)] [[PubMed](#)]
26. Wang, H.; Zhang, L.; Guo, X.; Dong, W.; Wang, R.; Shuang, S.; Gong, X.; Dong, C. Comparative study of Cl₂N-Cdots and N-Cdots and application for trinitrophenol and ClO^- sensor and cell-imaging. *Anal. Chim. Acta* **2019**, *1091*, 76–87. [[CrossRef](#)]
27. Wang, L.; Jana, J.; Chung, J.S.; Hur, S.H. High quantum yield aminophenylboronic acid-functionalized N-doped carbon dots for highly selective hypochlorite ion detection. *Spectrochim. Acta Part A Mol. Biomol. Spectrosc.* **2021**, *260*, 119895. [[CrossRef](#)]
28. Ma, L.; Sun, S.; Wang, Y.; Jiang, K.; Zhu, J.; Li, J.; Lin, H. A graphene quantum dot-based fluorescent nanoprobe for hypochlorite detection in water and in living cells. *Microchim. Acta* **2017**, *184*, 3833–3840. [[CrossRef](#)]
29. Meng, Y.; Zhang, H.; Li, W.; Liu, Y.; Gong, X.; Shuang, S.; Dong, C. A facile synthesis of long-wavelength emission nitrogen-doped carbon dots for intracellular pH variation and hypochlorite sensing. *Biomater. Sci.* **2021**, *9*, 2255–2261. [[CrossRef](#)]
30. Yan, F.; Bai, Z.; Ma, T.; Sun, X.; Zu, F.; Luo, Y.; Chen, L. Surface modification of carbon quantum dots by fluorescein derivative for dual-emission ratiometric fluorescent hypochlorite biosensing and in vivo bioimaging. *Sens. Actuators B Chem.* **2019**, *296*, 126638. [[CrossRef](#)]
31. Jiao, Y.; Meng, Y.; Lu, W.; Gao, Y.; Liu, Y.; Gong, X.; Liu, Y.; Shuang, S.; Dong, C. Design of long-wavelength emission carbon dots for hypochlorous detection and cellular imaging. *Talanta* **2020**, *219*, 121170. [[CrossRef](#)] [[PubMed](#)]
32. Hill, S.A.; Benito-Alifonso, D.; Davis, S.A.; Morgan, D.J.; Berry, M.; Galan, M.C. Practical three-minute synthesis of acid-coated fluorescent carbon dots with tuneable core structure. *Sci. Rep.* **2018**, *8*, 12234. [[CrossRef](#)]
33. Wang, C.-I.; Wu, W.-C.; Periasamy, A.P.; Chang, H.-T. Electrochemical synthesis of photoluminescent carbon nanodots from glycine for highly sensitive detection of hemoglobin. *Green Chem.* **2014**, *16*, 2509–2514. [[CrossRef](#)]
34. Wu, X.; Diao, Y.; Sun, C.; Yang, J.; Wang, Y.; Sun, S. Fluorimetric determination of ascorbic acid with o-phenylenediamine. *Talanta* **2003**, *59*, 95–99. [[CrossRef](#)]
35. Stejskal, J. Polymers of phenylenediamines. *Prog. Polym. Sci.* **2015**, *41*, 1–31. [[CrossRef](#)]
36. Liu, Z.X.; Wu, Z.L.; Gao, M.X.; Liu, H.; Huang, C.Z. Carbon dots with aggregation induced emission enhancement for visual permittivity detection. *Chem. Commun.* **2016**, *52*, 2063–2066. [[CrossRef](#)] [[PubMed](#)]
37. Sharma, A.; Gady, T.; Neogy, S.S.; Ghosh, K.; Kumbhakar, M. Molecular origin and self-assembly of fluorescent carbon nanodots in polar solvents. *J. Phys. Chem. Lett.* **2017**, *8*, 1044–1052. [[CrossRef](#)]
38. Zeng, Q.; Feng, T.; Tao, S.; Zhu, S.; Yang, B. Precursor-dependent structural diversity in luminescent carbonized polymer dots (CPDs): The nomenclature. *Light Sci. Appl.* **2021**, *10*, 142. [[CrossRef](#)]
39. Jiao, Y.X.; Han, G.H.; Gao, Y.; Lu, W.; Liu, Y.; Xian, M.; Shuang, S.; Dong, C. Facile synthesis of orange fluorescence carbon dots with excitation independent emission for pH sensing and cellular imaging. *Anal. Chim. Acta* **2018**, *1042*, 125–132. [[CrossRef](#)]
40. Craciun, A.M.; Diac, A.; Focsan, M.; Socaci, C.; Magyari, K.; Maniu, D.; Mihalache, I.; Veca, L.M.; Astilean, S.; Terec, A. Surface passivation of carbon nanoparticles with p-phenylenediamine towards photoluminescent carbon dots. *RSC Adv.* **2016**, *6*, 56944–56951. [[CrossRef](#)]
41. Vedamalai, M.; Periasamy, A.P.; Wang, C.-W.; Tseng, Y.-T.; Ho, L.-C.; Shih, C.-C.; Chang, H.-T. Carbon nanodots prepared from O-phenylenediamine for sensing of Cu^{2+} ions in cells. *Nanoscale* **2014**, *6*, 13119–13125. [[CrossRef](#)] [[PubMed](#)]

42. Dutta, A.; Trolles-Cavalcante, S.T.Y.; Cleetus, A.; Marks, V.; Schechter, A.; Webster, R.D.; Borenstein, A. Surface modifications of carbon nanodots reveal the chemical source of their bright fluorescence. *Nanoscale Adv.* **2021**, *3*, 716–724. [[CrossRef](#)]
43. Li, O.L.; Chiba, S.; Wada, Y.; Panomsuwan, G.; Ishizaki, T. Synthesis of graphitic-N and amino-N in nitrogen-doped carbon via a solution plasma process and exploration of their synergic effect for advanced oxygen reduction reaction. *J. Mater. Chem. A* **2017**, *5*, 2073–2082. [[CrossRef](#)]
44. Pillar-Little, T.; Kim, D.Y. Differentiating the impact of nitrogen chemical states on optical properties of nitrogen-doped graphene quantum dots. *RSC Adv.* **2017**, *7*, 48263–48267. [[CrossRef](#)]
45. Gupta, R.; Sanotra, S.; Sheikh, H.N.; Kalsotra, B.L. Room temperature aqueous phase synthesis and characterization of novel nano-sized coordination polymers composed of copper (II), nickel (II), and zinc (II) metal ions with p-phenylenediamine (PPD) as the bridging ligand. *J. Nanostruct. Chem.* **2013**, *3*, 41. [[CrossRef](#)]
46. Zhang, L.; Wang, H.; Yu, W.; Su, Z.; Chai, L.; Li, J.; Shi, Y. Facile and large-scale synthesis of functional poly (*m*-phenylenediamine) nanoparticles by Cu²⁺-assisted method with superior ability for dye adsorption. *J. Mater. Chem. A* **2012**, *22*, 18244–18251. [[CrossRef](#)]
47. Limosani, F.; Bauer, E.M.; Cecchetti, D.; Biagioni, S.; Orlando, V.; Pizzoferrato, R.; Proposito, P.; Carbone, M. Top-down N-doped carbon quantum dots for multiple purposes: Heavy metal detection and intracellular fluorescence. *Nanomaterials* **2021**, *11*, 2249. [[CrossRef](#)] [[PubMed](#)]
48. Takei, K.I.; Takahashi, R.; Noguchi, T. Correlation between the hydrogen-bond structures and the C=O stretching frequencies of carboxylic acids as studied by density functional theory calculations: Theoretical basis for interpretation of infrared bands of carboxylic groups in proteins. *J. Phys. Chem. B* **2008**, *112*, 6725–6731. [[CrossRef](#)] [[PubMed](#)]
49. Li, S.; Song, X.; Wang, Y.; Hu, Z.; Yan, F.; Feng, G. Developed a ratiometric fluorescence pH nanosensor based on label-free carbon dots for intracellular lysosome imaging and water pH monitoring with a smartphone. *Dyes Pigm.* **2021**, *193*, 109490. [[CrossRef](#)]
50. Song, S.; Hu, J.; Li, M.; Gong, X.; Dong, C.; Shuang, S. Fe³⁺ and intracellular pH determination based on orange fluorescence carbon dots co-doped with boron, nitrogen and sulfur. *Mater. Sci. Eng. C* **2021**, *118*, 111478. [[CrossRef](#)]
51. Ghosh, T.; Chatterjee, S.; Prasad, E. Photoinduced electron transfer from various aniline derivatives to graphene quantum dots. *J. Phys. Chem. A* **2015**, *119*, 11783–11790. [[CrossRef](#)]
52. Escudero, D. Revising intramolecular photoinduced electron transfer (PET) from first-principles. *Acc. Chem. Res.* **2016**, *49*, 1816–1824. [[CrossRef](#)]
53. Zhang, S.; Ji, X.; Liu, J.; Wang, Q.; Jin, L. One-step synthesis of yellow-emissive carbon dots with a large Stokes shift and their application in fluorimetric imaging of intracellular pH. *Spectrochim. Acta Part A Mol. Biomol. Spectrosc.* **2020**, *227*, 117677. [[CrossRef](#)] [[PubMed](#)]
54. Wang, Q.; Yang, H.; Zhang, Q.; Ge, H.; Zhang, S.; Wang, Z.; Ji, X. Strong acid-assisted preparation of green-emissive carbon dots for fluorometric imaging of pH variation in living cells. *Mikrochim. Acta* **2019**, *186*, 468. [[CrossRef](#)] [[PubMed](#)]
55. Shangguan, J.; He, D.; He, X.; Wang, K.; Xu, F.; Liu, J.; Tang, J.; Yang, X.; Huang, J. Label-free carbon-dots-based ratiometric fluorescence pH nanoprobe for intracellular pH sensing. *Anal. Chem.* **2016**, *88*, 7837–7843. [[CrossRef](#)] [[PubMed](#)]
56. Wei, Z.; Li, H.; Liu, S.; Wang, W.; Chen, H.; Xiao, L.; Ren, C.; Chen, X. Carbon dots as fluorescent/colorimetric probes for real-time detection of hypochlorite and ascorbic acid in cells and body fluid. *Anal. Chem.* **2019**, *91*, 15477–15483. [[CrossRef](#)] [[PubMed](#)]
57. Losada-Barreiro, S.; Bravo-Diaz, C. Free radicals and polyphenols: The redox chemistry of neurodegenerative diseases. *Eur. J. Med. Chem.* **2017**, *133*, 379–402. [[CrossRef](#)]
58. Nguema, P.; Jun, M. Application of ferrate (VI) as disinfectant in drinking water treatment processes: A review. *Int. J. Microbiol. Res.* **2016**, *7*, 53–62.
59. Berg, R.M.G.; Møller, K.; Bailey, D.M. Neuro-oxidative-nitrosative stress in sepsis. *J. Cereb. Blood Flow Metab.* **2011**, *31*, 1532–1544. [[CrossRef](#)]